Tuning structural and electronic properties of two-dimensional aluminum monochalcogenides: Prediction of Janus Al$_2XX'$ (X/X': O, S, Se, Te) monolayers

M. Demirtas,[1,2] M. Jahangirzadeh Varjovi,[1] M. M. Cicek,[1,3] and E. Durgun [1,*]

[1]*UNAM—National Nanotechnology Research Center and Institute of Materials Science and Nanotechnology, Bilkent University, Ankara 06800, Turkey*
[2]*Department of Physics, Kafkas University, 36100, Kars, Turkey*
[3]*Department of Engineering Physics, Faculty of Engineering, Ankara University, Ankara 06100, Turkey*

The realization of ternary, single-layer transition metal dichalcogenides has suggested a promising strategy to develop two-dimensional (2D) materials with alternative features. In this study, we design and investigate Janus aluminum monochalcogenide monolayers, Al$_2XX'$ ($X/X' =$ O, S, Se, and Te) by using first-principles methods. Starting from binary constituents, the ternary structures are optimized without any constraint and ground-state configurations are obtained. The stability of these systems is tested by performing phonon spectra analysis and *ab initio* molecular dynamics simulations and all Al$_2XX'$ monolayers other than AlTeO are confirmed to be dynamically stable. Mechanical properties are examined by calculating Young's modulus and Poisson's ratio and subsequently compared with binary counterparts. Monolayers of Al$_2XX'$ have a brittle character but oxygenation makes them less stiff. The electronic structure is also analyzed and variation of the band gap with the type of chalcogen atoms is revealed. It is found that different from their binary counterparts, Al$_2X$O monolayers are direct band-gap semiconductors. Additionally, modification of the electronic structure in the presence of biaxial compressive or tensile strain is investigated by taking into account possible indirect-direct band-gap transitions. Our results not only predict stable 2D ternary Al$_2XX'$ structures but also point out them as promising materials for optoelectronic applications.

I. INTRODUCTION

Consecutive to the isolation of graphene and uncovering its extraordinary properties [1], the dynasty of two-dimensional (2D) materials has expanded rapidly [2–4]. A realization of every new member suggests alternative features, holding the promise to be used in current and prospective nanodevices [5]. In this sense, recently the 2D group-III monochalcogenides have become the focus of numerous studies, as they possess remarkable electronic, optical, thermal, and mechanical properties [6,7]. Until now, 2D crystals of GaS [8–10], GaSe [11,12], GaTe [13,14], and InSe [15,16] have been synthesized and their unique properties have been characterized. Their possible applications such as photocatalysts for water splitting [17], field-effect transistors (FETs) [18], and solar photovoltaics [19] have also been proposed. In addition to experimental efforts, the entire class of group-III monochalcogenides (MX, $M =$ B, Al, Ga, In; $X =$ O, S, Se, Te) have been examined by first-principles methods and stable structures among them have been predicted [20]. MX monolayers are semiconductors with indirect band gaps, which span a wide range from deep ultraviolet to near infrared [20,21]. It has been shown that along with GaX, an unusual band inversion (Mexican-hat dispersion) [21,22] is also noticed in monolayers of AlX, the class of which should be further analyzed. Recently, it has been reported that AlX monolayers exhibit outstanding thermoelectric performance, which make them promising candidate matrices in high efficiency thermoelectric nanocomposites [23]. Additionally, nanosheets of aluminum oxides have been found to be dynamically stable [24,25], indicating the possible realization of AlX systems in the near future.

In parallel with the attempts on exploring new 2D systems, the formation of ternary (Janus) configurations has been suggested as an alternative approach to tailor the inherent properties of already existing 2D structures [26,27]. Recently, the growth of Janus SMoSe monolayers by replacing one of the S layers with Se (or vice versa) has been reported [26,28]. This development has been followed by fabrication [29–32] and prediction [33–36] of a variety of ternary transition metal dichalcogenides (TMDs). The research on Janus 2D systems is not limited to TMDs but also extended to other classes involving MX monolayers. In this regard, computational studies have revealed that Ga$_2XX'$ can be designed and utilized in many applications such as ultraviolet photodetectors [37] and piezoelectric materials [38] as well as photocatalytic water splitting [39]. Furthermore, oxygenation of gallium monochalcogenides (Ga$_2X$O) has been investigated and it has been demonstrated that while GaX monolayers are indirect band-gap semiconductors, Ga$_2X$O monolayers have direct band gaps and oxygenation also tuned their mechanical properties [40]. In another study, the stability of In$_2$SSe Janus monolayer has been predicted and a tunable direct band gap

*durgun@unam.bilkent.edu.tr

TABLE I. The lattice constant (**a**), bond lengths (d_{Al-Al}, d_{Al-X}, and $d_{Al-X'}$), thickness (h), bond angle between X-Al-X and X-Al-X' (θ and θ'), cohesive energy per atom (E_C), electronic band gap at the level of PBE and HSE (E_g^{PBE} and E_g^{HSE}), Poisson's ratio (ν), in-plane stiffness (Y_{2D}), electronegativity difference ($\Delta\chi$), and average charge transfer from Al to X/X' ($\Delta\rho$) for monolayers of AlX and Al$_2XX'$. * indicates that no feature is calculated for that case.

Type	a (Å)	d_{Al-Al} (Å)	d_{Al-X} (Å)	$d_{Al-X'}$ (Å)	h (Å)	θ (deg)	θ' (deg)	E_C (eV)	E_G^{PBE} (eV)	E_G^{HSE} (eV)	ν —	Y_{2D} (J/m²)	$\Delta\chi$ —	$\Delta\rho$ (e^-)
AlO	2.87	2.61	1.80	1.80	4.01	105.9	105.9	5.67	1.06	1.61	0.36	155.0	1.83	1.69
Al$_2$SO	3.28	2.61	2.24	1.96	4.34	94.0	113.1	4.76	1.71	2.63	0.28	111.3	1.40	1.60
Al$_2$SeO	3.46	2.60	2.38	2.05	4.36	92.9	115.1	4.44	0.94	1.66	0.30	94.0	1.38	1.54
AlS	3.58	2.60	2.32	2.32	4.73	100.6	100.6	4.22	2.09	2.88	0.25	79.9	0.97	1.49
Al$_2$SSe	3.71	2.58	2.36	2.45	4.77	103.4	98.4	4.03	1.97	2.74	0.25	74.1	0.95	1.44
AlSe	3.78	2.58	2.47	2.47	4.91	99.6	99.6	3.87	2.00	2.73	0.24	68.3	0.94	1.39
Al$_2$TeO	3.79	2.58	2.61	2.21	5.78	93.0	117.5	3.84	0.58	1.07	*	*	1.16	1.42
Al$_2$STe	3.96	2.57	2.45	2.65	4.79	108.1	96.5	3.65	1.57	2.23	0.24	64.4	0.73	1.35
Al$_2$SeTe	4.06	2.57	2.56	2.68	4.90	104.9	98.4	3.53	1.58	2.35	0.23	60.3	0.72	1.29
AlTe	4.11	2.57	2.70	2.70	5.13	99.4	99.4	3.28	1.84	2.48	0.24	55.0	0.49	1.22

under strain has been reported [41]. These studies have indicated that the addition of a third element and broken structural symmetry can lead to new and more interesting features which exhibit great potential for numerous applications [42–44].

In accordance with recent advancements in ternary 2D systems, in this paper, we design and investigate the monolayers of Al$_2XX'$ (X/X': O, S, Se, and Te) which is one of the prominent group within MX. First, we design Al$_2XX'$ monolayers and optimized them without any constraint to obtain ground-state configurations. Next, the dynamical stability of the monolayers is explored with phonon spectrum analysis and *ab initio* molecular dynamics simulations. Revealing the stability, the mechanical properties are examined and in-plane stiffness (Y_{2D}) and Poisson's ratio (ν) are calculated. Finally, the electronic properties are studied and the effect of strain on electronic band structures is reported. For each case, the variation of the obtained properties with the type of X/X' is illustrated and compared with binary AlX monolayers.

II. METHODOLOGY

We performed first-principles calculations based on density-functional theory (DFT) [45,46] as implemented in the Vienna *Ab initio* Simulation Package (VASP) [47–50]. The projector augmented wave (PAW) [51] method was utilized to portray the potentials of Al, O, S, Se, and Te elements. The exchange-correlation term was described within the generalized gradient approximation (GGA) as parameterized by Perdew-Burke-Ernzerhof (PBE) [52]. In addition to GGA-PBE, Heyd-Scuseria-Ernzerhof (HSE06) hybrid functional was adopted to correct the underestimated electronic band gaps [53,54]. A plane-wave basis set with a cutoff energy of 530 eV was taken. The Γ-centered $16 \times 16 \times 1$ uniform k-point mesh was used to sample the Brillouin zone [55]. A vacuum space of ~20 Å was employed to hinder any interaction in the nonperiodic direction. All ionic positions and lattice constants were relaxed until the force on each atom was less than 0.01 eV/Å. The convergence criterion for electronic steps was set to 10^{-5} eV. The phonon spectrum analyses were carried out for $6 \times 6 \times 1$ supercell by using the finite displacement method which is implemented in the

PHONOPY package [56]. To analyze the thermal stability of the considered structures, *ab initio* molecular dynamics (AIMD) calculations were performed for $6 \times 6 \times 1$ supercell considering microcanonical ensemble simulation at elevated temperatures. Bader charge analysis was used to estimate the charge transfers between the atoms [57].

III. RESULTS AND DISCUSSION

A. Structural properties and energetics

We start with the structural optimization of binary AlX (X: O, S, Se, Te) monolayers. The geometry of AlX belongs to the D_{3h} symmetry group and consists of four sublayers (X-Al-Al-X) which are held together with strong covalent bonds [20]. The Al planes are surrounded by two chalcogen layers exhibiting mirror symmetry in the vertical direction. The calculated structural parameters of the binary systems, which are in good agreement with the literature, are summarized in Table I [17,20].

After obtaining the binary systems, one of the X layers is fully replaced with a different chalcogen atom (X') to design the Janus Al$_2XX'$ (X/X': O, S, Se, Te) monolayer. The prototype structure is shown in Fig. 1. Taking account the broken symmetry in z direction, the lattice constants (**a** and **b**) are relaxed separately, but found to be equal. This indicates that the hexagonal lattice is also preserved in ternary systems. The calculated structural parameters, which are lattice constants (**a**), bond length between Al-Al (d_{Al-Al}), Al-X (d_{Al-X}), Al-X'
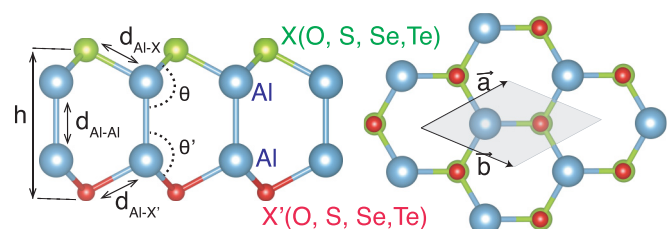
FIG. 1. Top and side views of the prototype structure of the predicted ternary Al$_2XX'$ monolayers. The relevant structural parameters are shown.
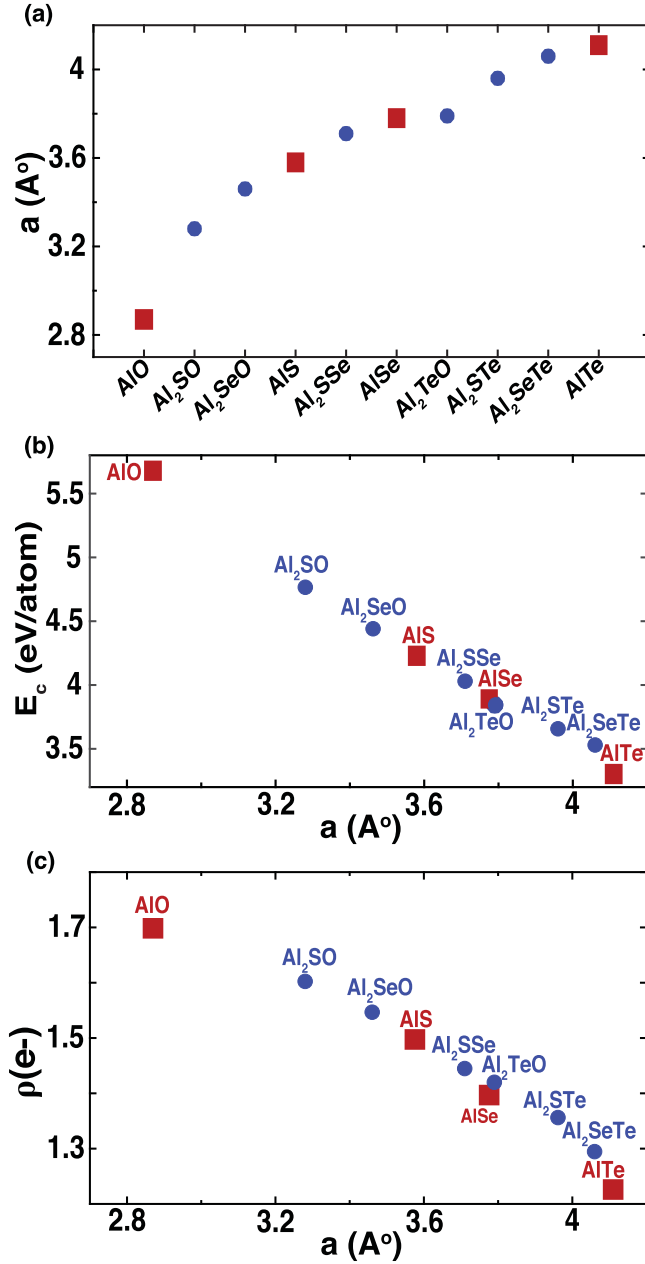
FIG. 2. (a) The distribution of lattice constant (**a**) for all the considered Al_2XX' and AlX monolayers, (b) the variation of cohesive energy (E_c), and (c) the average charge transfer (ρ) from Al to chalcogenide atoms with the lattice constant.

($d_{Al-X'}$), thickness (h), and the angle between Al and X/X' atoms (θ and θ') for both binary AlX and ternary Al_2XX', are summarized in Table I. It is found that for fixed X, the structural parameters of Al_2XX' vary regularly with the size of X' and the obtained results are the average of AlX and AlX'. Accordingly, all parameters are analyzed with respect to the type of X' for a given subset of X throughout the study.

The distribution of **a** for all the considered binary and ternary systems is shown in Fig. 2(a). Accordingly, it turns out that **a** increases down the group of X' for each subset of X. As an example, for $X = S$, **a** follows a sequence of Al_2SO < Al_2SS < Al_2SSe < Al_2STe and a similar relation holds

for the other choices of X following a similar trend for AlX. In coherence with **a**, d_{Al-X} and $d_{Al-X'}$ also elongate and h thickens with the size of X'. On the other hand d_{Al-Al} slightly shortens with increasing **a** and this is related to decreasing charge transfer from Al atoms to X and/or X'.

The cohesive energy per atom (E_C) can be calculated by using the following relation:

$$E_C = \frac{N_{Al}E_{Al} + N_X E_X + N_{X'}E_{X'} - E_{Al_2XX'}}{N_{Al} + N_X + N_{X'}} \quad (1)$$

where $E_{Al_2XX'}$ is the total energy of the Al_2XX' monolayer; E_{Al}, E_X, $E_{X'}$ (N_{Al}, N_X, $N_{X'}$) are the single atom energies (total number) of Al, X, X' elements, respectively. As shown in Fig. 2(b), there is an inverse proportion between E_C and **a**, and cohesive energy decreases down the group of X'. The elongation of **a** together with d_{Al-X} and $d_{Al-X'}$ indicates bond weakening and explains the descent in E_C. Additionally, as shown in Fig. 2(c) the average charge donated by Al atoms ($\Delta\rho$) decreases with increasing **a** associated with the electronegativity difference ($\Delta\chi$) between X/X' and Al (Table I) and supports the variation of E_C. The isolation of AlO (and Al_2XO) from other binary (ternary) monolayers [20] is correlated with the very high χ of oxygen atom [58]. When compared with their binary counterparts, E_C of Al_2XX' lies between those of AlX and AlX'.

It should also be noted that Janus Al_2XX' structure is not only the possible ordered alloy morphology. However, this configuration is chosen intentionally following the realized 2D ternary systems [26,28], we also examined other possible structures (see Fig. S1 and Table S1 in the Supplemental Material [59]). Interestingly, Janus geometry is energetically the most favorable phase except Al_2TeO.

B. Dynamical stability

After revealing the structural features, the dynamical stability of Al_2XX' monolayers is examined firstly by calculation of the phonon dispersion spectra as shown in Fig. 3. Except Al_2TeO, the phonon frequencies are found to be real for the considered structures indicating the stability at low temperature. The instability of Al_2TeO results from the strong asymmetry in the accumulated charge on O and Te due to the large electronegativity difference between these atoms. Similar result was also reported for Ga_2TeO monolayer [40].

Phonon spectra not only provide information about stability of the structures but also they help to analyze the eigenmodes. The primitive cell of Al_2XX' monolayer contains four atoms, resulting in twelve phonon branches, three of which are acoustic and the rest are optical. The symmetry of Al_2XX' is described by $P3m1$ space group (C_{3v} point group). Accordingly, the optical phonon modes at the Γ point are expected to be either nondegenerate or doubly degenerate. The group theory analysis reveals that the corresponding irreducible representation for phonon modes in the spectrum is given by $\Gamma = 3E + 3A_1$, where all E phonon modes are attributed to the doubly degenerate in-plane vibrations whereas all nondegenerate A_1 phonon modes represent vibrations along the z direction. E and A_1 modes are both infrared and Raman active as these modes correspond to the linear and quadratic functions in C_{3v} symmetry. Therefore,
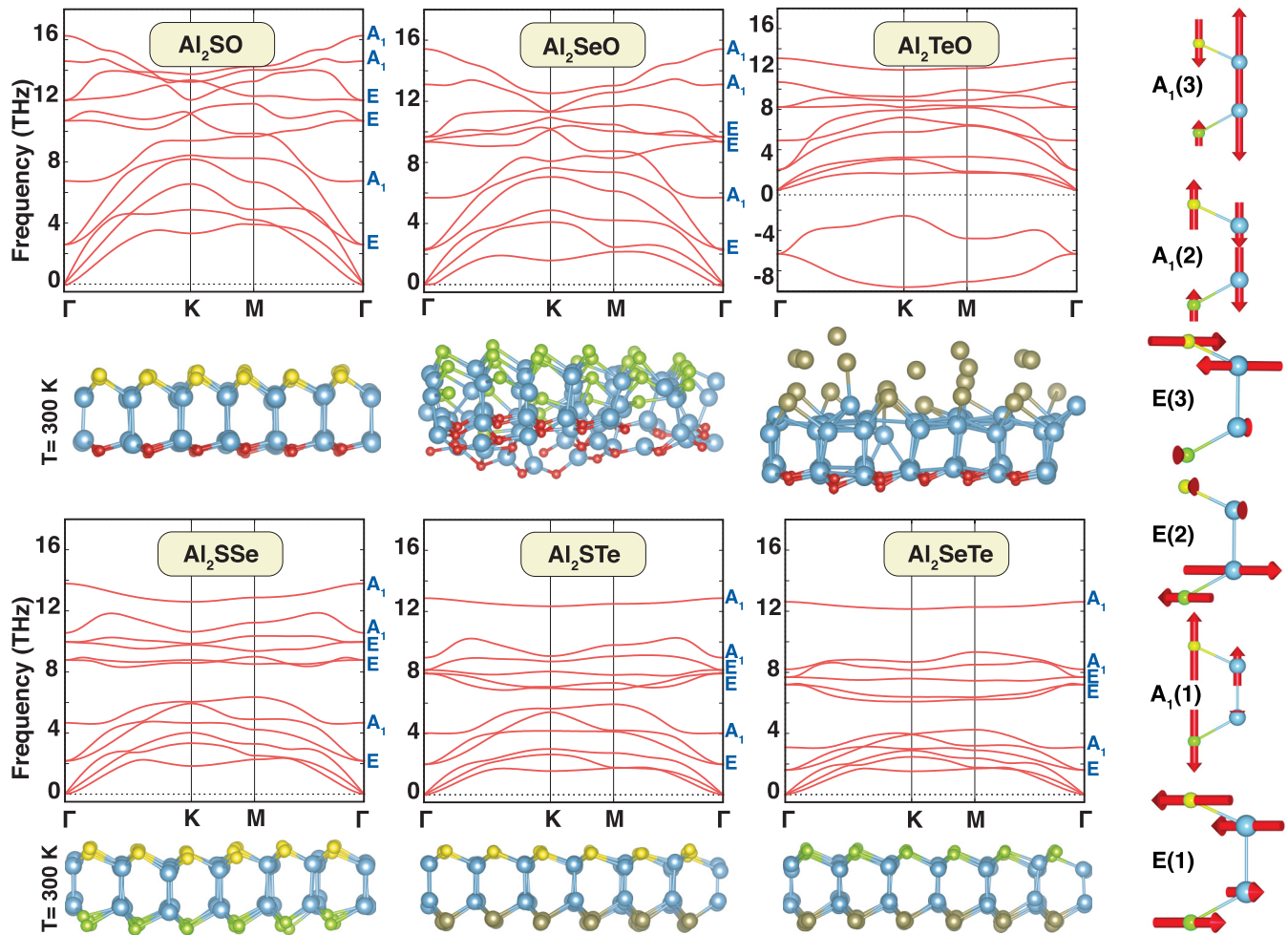
FIG. 3. Phonon dispersion diagrams and AIMD simulation snapshots at $T = 300$ K. The blue, yellow, green, brown, and red spheres represent Al, S, Se, Te, and O atoms, respectively. The representative eigenvectors calculated at Γ point are also shown. The red arrows on the atoms demonstrate the eigenmodes.

Al$_2XX'$ monolayers should exhibit six peaks at Raman- and six peaks at IR spectrum. The atomic displacements of six distinct phonon modes are illustrated in Fig. 3. As X and X' have different atomic masses, the vibrations of AlX and AlX' pairs are not symmetric. The first optical mode with the lowest frequency is owned by E representation. In this mode, AlX pair moves in the opposite in plane direction of AlX' pair. The first E mode is followed by A_1 mode and in this mode, AlX and AlX' pairs vibrate in the opposite out of plane direction. In the higher segment of the phonon spectrum, there are two doubly degenerate E modes and their energies are very close to each other. For the second E mode, the vibration of AlX' pair is significantly larger than the AlX while Al and X' atoms vibrate in the opposite in plane direction. The same trend can be found for the third E mode. However, in this mode, the vibration of AlX' is smaller than AlX pair and can be ignored. The character of the second A_1 mode reveals that each of the four atomic planes in the monolayer vibrates in the opposite out of plane direction. Finally, when the eigenvectors of the third nondegenerate A_1 mode are analyzed, it is found that Al atoms and X/X' atoms move in the opposite direction along z axis while the vibrations of Al atoms dominate those of the chalcogenide atoms. Additionally, it is noticed that the phonon

modes are softened when the average atomic mass increases as seen in Fig. 3. Similarly to the AlX monolayers, the highest frequency phonon band originated from the Al atoms. While the phonon modes of Al$_2X$O monolayers are interwoven, a gap is noticed between lower and higher frequency optical branches for Al$_2$SSe, Al$_2$STe, and Al$_2$SeTe. The bond strength and the mass differences between the constitute atoms in the Al$_2XX'$ monolayers are the origins of the phonon band gaps. Recently, it has been shown that phonon band gaps play an important role in determining and controlling thermal conductivity through material design [60,61]. In this respect, low thermal conductivity is expected for Al$_2X$O systems due to strong acoustic and optical scattering [62,63].

We further explore the high temperature stability by performing AIMD simulations. To alter the unit cell constraint, a $6 \times 6 \times 1$ super cell is constructed for all models and simulations are performed at $T = 300$ K and 600 K within 2 ps total simulation time. The final snapshots of the resulting geometries are represented in Fig. 3. For Al$_2$TeO, Te atoms detached from the system at 300 K and thus the ternary structure is destroyed confirming the phonon spectrum results. Although the Al$_2$SeO appears to be stable according to all real phonon modes, the structure deforms at 300 K, indicating a plausible
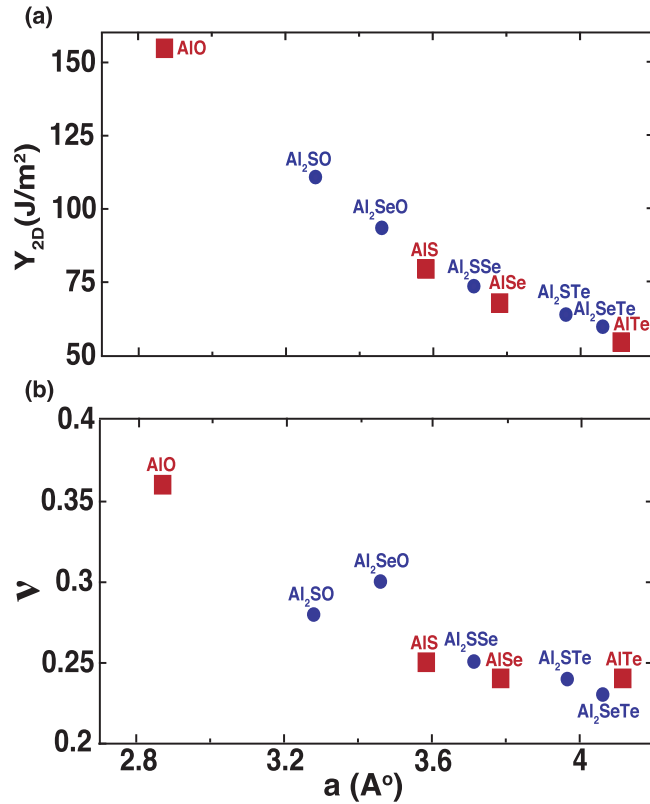
FIG. 4. (a) The variation of in plane stiffness (Y_{2D}) and (b) Poisson's ratio (ν) with the lattice constant of Al_2XX' and AlX monolayers.

instability at elevated temperatures. For the case of Al_2SO, the last member of Al_2XO, the structure preserves its geometry up to 600 K, but small distortions are noticed. On the other hand, Al_2SSe, Al_2STe, and Al_2SeTe maintain their structures even at high temperatures. Accordingly, it can be concluded that oxygenation weakens the strength of the bonds and can induce instability in ternary monolayers. In addition, although the stability at ambient conditions can be assumed based on experimental studies on GaX systems [64–66], further investigation (i.e., stability against oxidation) [67] is required to reveal this issue for practical applications.

C. Mechanical properties

After revealing the stability of the predicted structures, the elastic constants (C_{ij}) tensor is calculated to obtain the mechanical properties by following the stress theorem [68,69]. C_{ij}'s are found to be positive for all Al_2XX' monolayers other than Al_2TeO, fulfilling the Born stability criterion. The results for Al_2TeO are anticipated as its instability has already been demonstrated by phonon dispersion analysis and AIMD simulations. Accordingly, no mechanical feature is examined for Al_2TeO. Firstly, in plane stiffness Y_{2D}, which is the measure of the rigidity, is calculated. For a hexagonal lattice [70], it can be obtained with the following formula; $Y_{2D} = (C_{11}^2 - C_{12}^2)/C_{11}$. As shown in Fig. 4(a), Y_{2D} decreases with the elongation of a. This can be associated with the reduction of bond strength among the atoms since E_C also follows a similar trend. Additionally, for the designated X, Y_{2D} decreases down the group

of X'. Al_2OX' monolayers have higher Y_{2D} than the other Janus structures as the AlO sets the upper limit. Similarly to structural features, Y_{2D} of Al_2XX' is in between that of binary counterparts. It should be noted that Y_{2D} can be converted to bulk units by dividing it with effective thickness [70].

Next, the Poisson's ratio is calculated by utilizing the relation; $\nu = C_{12}/C_{11}$. Although to a lesser extent, ν also decreases with elongation of a as shown in Fig. 4(b). As $\nu < 1/3$ for all cases, it can be concluded that Al_2XX' monolayers are brittle according to the Frantsevich rule [71]. Similarly to Y_{2D}, ν of Al_2OX' are larger than those of the other systems. In other words, as only AlO has a ductile character with $\nu = 0.36$, the oxygenation makes AlX monolayers less stiff.

D. Electronic properties

Finally, the electronic properties of AlX and Al_2XX' monolayers are investigated. The electronic band structures and orbital projected density of states of AlX are shown in Figs. S2 and S3 (see the Supplemental Material [59]). It should be noted that the precursor AlX monolayers are indirect band-gap semiconductors [20]. AlO has a different electronic band profile among other binary structures and has the narrowest band gap. While the highest valence band (HVB) is localized and mainly composed of Al-p_z and X-p_z orbitals for AlS, AlSe, and AlTe, HVB is very dispersive for AlO and in addition to Al-p_z and O-p_z orbitals, significant contribution from O-s orbital is noticed. This feature can be clarified by band-decomposed charge analysis [20]. While the electronic states of AlO at the K point are accumulated between Al atoms and have a σ character, the states at the Γ point concentrated around O atoms and have a π character. Accordingly, the states at Γ point have lower energy with respect to K point due to $\Delta\chi$ between Al and O atoms. On the other hand, the lowest conduction band (LCB) is dispersive with two valleys at K and M points (Mexican-hat dispersion) [22] and has a similar character for all AlX systems. This type of band dispersion induces Fermi ring of states, which can give rise to unique features including itinerant magnetism and superconductivity [72].

Revealing the electronic properties of binary systems, the electronic band structures Al_2XX' monolayers are calculated and shown in Fig. 5. While all the precursor AlX monolayers are indirect band-gap semiconductors, indirect to direct band-gap transition is noticed for Al_2XO. The same trend was also reported for Ga_2XO [40]. This transition is induced first due to the dramatic modification of HVB with inclusion of oxygen (see above). Secondly, the first and second LCB has multiple valleys at high symmetry points and when the intrinsic strain (two surfaces are under different types of induced biaxial strains, i.e., the O side undergoes tensile strain whereas the X side is compressed) is large enough, it not only shifts the bands but also alters the order of band extremums. Accordingly, for Al_2XO monolayers, because of these two affects, valence band maximum and conduction band minimum are shifted to Γ point and system turns into a direct band-gap semiconductor. The indirect-direct (or vice versa) transition is also reported for other Janus system [41,73]. For the remaining Al_2XX' monolayers, systems remain to be indirect band-gap semiconductors (for Al_2STe, the difference between
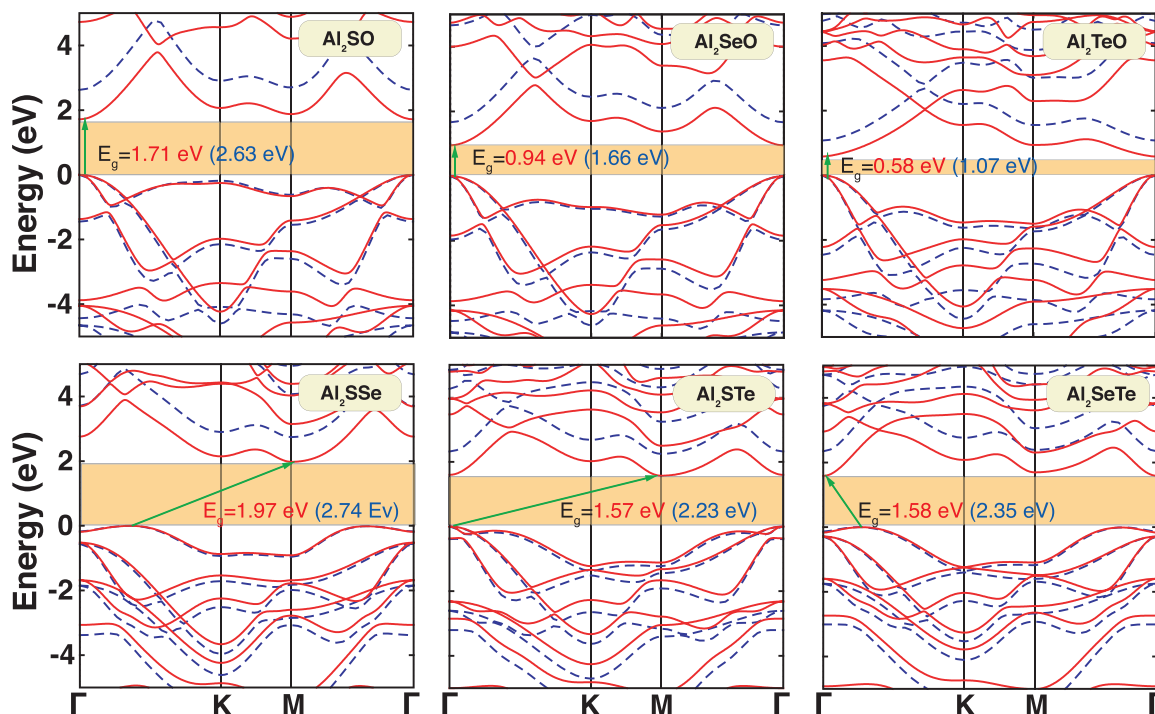
FIG. 5. The electronic band structures calculated at the level of GGA-PBE (red solid lines) and HSE06 (dashed blue lines) for Al_2XX' monolayers. The band-gap values, E_g^{PBE} (E_g^{HSE}) are shown with blue (red). The Fermi level is set to zero.

the indirect and direct band gap is reduced to ∼25 meV, and it can also be considered as a direct band-gap material at the ambient conditions). The electronic band structure features resemble their binary constituents and Mexican-hat dispersion is preserved. HVB is mainly composed of Al-, X-, and X'-p_z and in LCB contribution from Al-s orbital is noticed in addition to p_z orbitals (see Fig. S4 in the Supplemental Material [59]).

The variation of E_g^{PBE} and E_g^{HSE} with a is shown in Fig. 6. Different from other features, an apparent trend with respect to a is not noticed. As discussed above, the band profile is significantly influenced by inclusion of O atoms for Al_2XO, and also by the intrinsic strain on both sides due to the broken symmetry, thus the alternation of E_g cannot be classified simply with the type of X atom. Moreover, while the calculated features for Janus monolayers are the average of their binary constituents, E_g does not fit in this trend, E_g of Al_2XX' can be even narrower than AlX and AlX'.
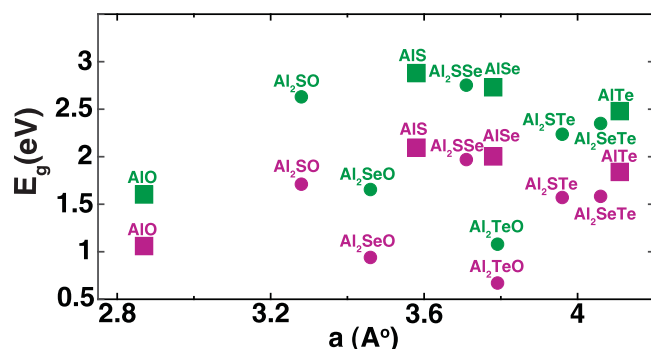
FIG. 6. The variation of E_g^{PBE} (in purple) and E_g^{HSE} (in green) with lattice constant values.

As the effect of intrinsic strain on the electronic structure is found to be substantial, we also examine the variation of E_g^{PBE} with compressive or tensile biaxial strain for both AlX and Al_2XX' monolayers, and the results are shown in Fig. 7. The nonmonotonic variation of E_g^{PBE} under strain can be revealed by examining the change of bands in the vicinity of Fermi level (E_F). The strain dependent electronic band structures for binary systems are represented in Figures S5, S6, S7, and S8 (see the Supplemental Material [59]). For AlS, AlSe, and AlTe, while HVB is not significantly affected by tensile strain, the energy of LCB is lowered, resulting in a bang gap narrowing. It should also be mentioned that conduction band edge at Γ point is lowered with tensile strain and the energy difference between M point is closed gradually. On the other hand, E_g^{PBE} increases up to −2% as it is expected but then starts to decrease beyond this level. The compressive strain not only shifts LCB but also alters the energy levels of valleys (band extremums) at high symmetry points. Conduction band minimum is switched from K to M points and band gap narrows once again. While the effect of strain is more dramatic for AlTe, it is less significant for AlS, and this can be associated with the bond strength. AlO behaves differently then the other monolayers; E_g widens with tensile strain whereas a narrowing is anticipated. This is correlated with the dispersive HVB which is the distinctive feature of AlO. While the effect of tensile strain on LCB is similar to other binary monolayers, the dispersion of HVB is altered significantly and becomes less dispersive. The combined effect gives rise to an increase in E_g.

Accordingly, the complex effect of strain on electronic structure of Al_2XX' can be explained by comparison with binary AlX monolayers. The strain dependent electronic band structures of ternary monolayers are shown in Figures
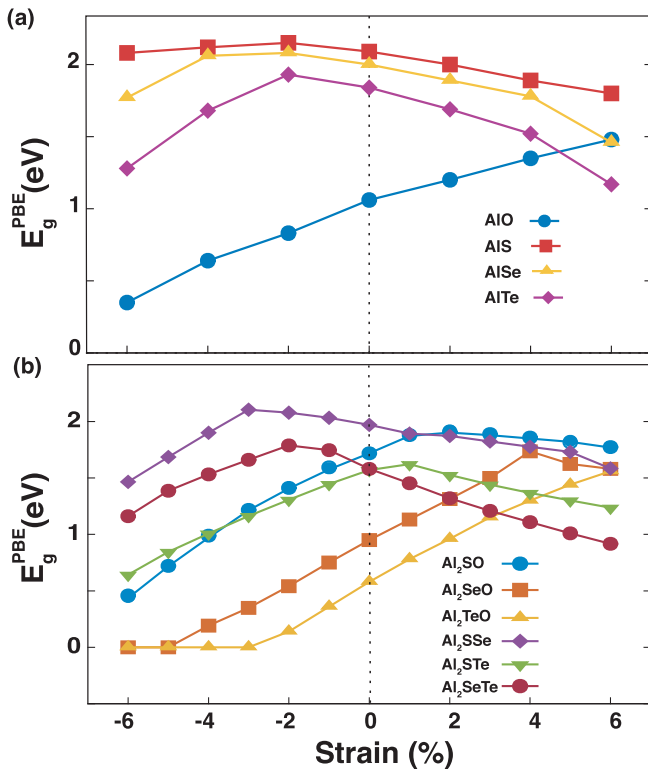
FIG. 7. The variation of E_g^{PBE} of (a) AlX and (b) Al$_2XX'$ monolayers under compressive ($-$) and tensile ($+$) biaxial strain.

S9, S10, S11, S12, S13, and S14 (see the Supplemental Material [59]). Whereas the variation of E_g for Al$_2$SeO and Al$_2$TeO resembles AlO, that of Al$_2$SO is a combination of AlS and AlO. The oxygenation of AlS makes it more sensitive to strain, and E_g of Al$_2$SO narrows dramatically with increasing tensile strain. The irregular pattern above -3% for Al$_2$TeO (-5% for AlSeO) can be linked with the structural instability. As discussed above, the intrinsic strain is stated as one of factors that leads to indirect to direct band-gap transition in Al$_2X$O. In a similar manner, direct to indirect transition is noticed in Al$_2X$O monolayers with applied strain. As illustrated in Figs. S9, S10, and S11 (see the Supplemental Material [59]), the valence band maximum (and conduction band minimum) switches from Γ to $\Gamma - K$ (Γ to K or M) with strain and alters the direct band-gap

character. On the other side, E_g of Al$_2$SSe, Al$_2$STe, and Al$_2$SeTe follow a similar trend to that of AlSe (or AlTe). These results indicate that the electronic structure of Al$_2XX'$ is sensitive to elongation or contraction of **a** and their E_g can be easily modified by applied strain.

IV. CONCLUSION

In conclusion, we design and analyze the monolayers of Al$_2XX'$ (X/X': O, S, Se, Te). Our stability analyses, performed by phonon dispersion calculations and AIMD simulations, indicate that while Al$_2$TeO is dynamically unstable, and Al$_2$SeO is prone to instability at elevated temperatures, the other predicted Janus systems are stable at ambient conditions. The calculated cohesive energies of Al$_2XX'$ are in between their binary constituents and they decrease with elongation of the lattice constant due to weakening of the bonds and reduced charge transfer between Al and X/X' atoms. The Young's modulus of Al$_2XX'$ decreases down the group of X' for a given X subset following the same trend with cohesive energy. All calculated Poisson's ratios are less than 1/3 indicating a brittle character, but oxygenation makes Al$_2XX'$ monolayers less stiff. Similar to their binary counterparts, ternary monolayers are also semiconductors but indirect to direct band-gap transition is noticed for Al$_2X$O and Al$_2$STe as a result of anisotropic strain on both sides of the Janus structures. However, the variation of band gap does not follow a regular pattern; it is found to be very sensitive to strain and thus can be easily tuned by the applied compressive or tensile strain. Our results indicate that with the design of Al$_2XX'$ structures, stable monolayers with direct band gap (lying within the visible spectrum) can be realized and such systems can be ideal materials to be utilized in diverse optoelectronic applications.

[1] K. S. Novoselov, A. K. Geim, S. V. Morozov, D. Jiang, Y. Zhang, S. V. Dubonos, I. V. Grigorieva, and A. A. Firsov, Science **306**, 666 (2004).

[2] P. Miró, M. Audiffred, and T. Heine, Chem. Soc. Rev. **43**, 6537 (2014).

[3] S. Z. Butler, S. M. Hollen, L. Cao, Y. Cui, J. A. Gupta, H. R. Gutiérrez, T. F. Heinz, S. S. Hong, J. Huang, A. F. Ismach *et al.*, ACS Nano **7**, 2898 (2013).

[4] C. Tan, X. Cao, X.-J. Wu, Q. He, J. Yang, X. Zhang, J. Chen, W. Zhao, S. Han, G.-H. Nam *et al.*, Chem. Rev. **117**, 6225 (2017).

[5] T. Das and J.-H. Ahn, FlatChem **3**, 43 (2017).

[6] K. Xu, L. Yin, Y. Huang, T. A. Shifa, J. Chu, F. Wang, R. Cheng, Z. Wang, and J. He, Nanoscale **8**, 16802 (2016).

[7] W. Huang, L. Gan, H. Li, Y. Ma, and T. Zhai, CrystEngComm **18**, 3968 (2016).

[8] S. Yang, Y. Li, X. Wang, N. Huo, J.-B. Xia, S.-S. Li, and J. Li, Nanoscale **6**, 2582 (2014).

[9] A. Harvey, C. Backes, Z. Gholamvand, D. Hanlon, D. McAteer, H. C. Nerl, E. McGuire, A. Seral-Ascaso, Q. M. Ramasse, N. McEvoy *et al.*, Chem. Mater. **27**, 3483 (2015).

[10] P. Hu, L. Wang, M. Yoon, J. Zhang, W. Feng, X. Wang, Z. Wen, J. C. Idrobo, Y. Miyamoto, D. B. Geohegan *et al.*, Nano Lett. **13**, 1649 (2013).

[11] P. Hu, Z. Wen, L. Wang, P. Tan, and K. Xiao, ACS Nano **6**, 5988 (2012).

[12] S. Lei, L. Ge, Z. Liu, S. Najmaei, G. Shi, G. You, J. Lou, R. Vajtai, and P. M. Ajayan, Nano Lett. **13**, 2777 (2013).

[13] Z. Wang, K. Xu, Y. Li, X. Zhan, M. Safdar, Q. Wang, F. Wang, and J. He, ACS Nano **8**, 4859 (2014).

[14] F. Liu, H. Shimotani, H. Shang, T. Kanagasekaran, V. Zolyomi, N. Drummond, V. I. Fal'ko, and K. Tanigaki, ACS Nano **8**, 752 (2014).

[15] W. Feng, X. Zhou, W. Q. Tian, W. Zheng, and P. Hu, Phys. Chem. Chem. Phys. **17**, 3653 (2015).

[16] M. Wu, J.-j. Shi, M. Zhang, Y.-m. Ding, H. Wang, Y.-l. Cen, and J. Lu, Nanoscale **10**, 11441 (2018).

[17] H. L. Zhuang and R. G. Hennig, Chem. Mater. **25**, 3232 (2013).

[18] D. J. Late, B. Liu, J. Luo, A. Yan, H. R. Matte, M. Grayson, C. Rao, and V. P. Dravid, Adv. Mater. **24**, 3549 (2012).

[19] K. Cheng, Y. Guo, N. Han, X. Jiang, J. Zhang, R. Ahuja, Y. Su, and J. Zhao, Appl. Phys. Lett. **112**, 143902 (2018).

[20] S. Demirci, N. Avazlı, E. Durgun, and S. Cahangirov, Phys. Rev. B **95**, 115409 (2017).

[21] V. Zólyomi, N. D. Drummond, and V. I. Fal'ko, Phys. Rev. B **87**, 195403 (2013).

[22] T. Stauber, N. M. R. Peres, F. Guinea, and A. H. Castro Neto, Phys. Rev. B **75**, 115425 (2007).

[23] X. Chen, Y. Huang, J. Liu, H. Yuan, and H. Chen, ACS Omega **4**, 17773 (2019).

[24] T. T. Song, M. Yang, J. W. Chai, M. Callsen, J. Zhou, T. Yang, Z. Zhang, J. S. Pan, D. Z. Chi, Y. P. Feng *et al.*, Sci. Rep. **6**, 29221 (2016).

[25] S. Lin, Y. Wang, and Z. Chen, Front. Phys. **13**, 138109 (2018).

[26] J. Zhang, S. Jia, I. Kholmanov, L. Dong, D. Er, W. Chen, H. Guo, Z. Jin, V. B. Shenoy, L. Shi *et al.*, ACS Nano **11**, 8192 (2017).

[27] T. Gao, Q. Zhang, L. Li, X. Zhou, L. Li, H. Li, and T. Zhai, Adv. Opt. Mater. **6**, 1800058 (2018).

[28] A.-Y. Lu, H. Zhu, J. Xiao, C.-P. Chuu, Y. Han, M.-H. Chiu, C.-C. Cheng, C.-W. Yang, K.-H. Wei, Y. Yang *et al.*, Nat. Nanotechnol. **12**, 744 (2017).

[29] L. Li, P. Gong, W. Wang, B. Deng, L. Pi, J. Yu, X. Zhou, X. Shi, H. Li, and T. Zhai, ACS Nano **11**, 10264 (2017).

[30] Q. Jia, Y. C. Zhang, J. Li, Y. Chen, and B. Xu, Mater. Lett. **117**, 24 (2014).

[31] J. Wu, H. Yuan, M. Meng, C. Chen, Y. Sun, Z. Chen, W. Dang, C. Tan, Y. Liu, J. Yin *et al.*, Nat. Nanotechnol. **12**, 530 (2017).

[32] J.-U. Lee, S. Lee, J. H. Ryoo, S. Kang, T. Y. Kim, P. Kim, C.-H. Park, J.-G. Park, and H. Cheong, Nano Lett. **16**, 7433 (2016).

[33] W. Shi and Z. Wang, J. Phys. Condens. Matter. **30**, 215301 (2018).

[34] L. Dong, J. Lou, and V. B. Shenoy, ACS Nano **11**, 8242 (2017).

[35] F. Li, W. Wei, P. Zhao, B. Huang, and Y. Dai, J. Phys. Chem. Lett. **8**, 5959 (2017).

[36] A. Mogulkoc, Y. Mogulkoc, S. Jahangirov, and E. Durgun, J. Phys. Chem. C **123**, 29922 (2019).

[37] H. D. Bui, H. R. Jappor, and N. N. Hieu, Superlattice. Microst. **125**, 1 (2019).

[38] Y. Guo, S. Zhou, Y. Bai, and J. Zhao, Appl. Phys. Lett. **110**, 163102 (2017).

[39] R. da Silva, R. Barbosa, R. R. Mançano, N. Durães, R. B. Pontes, R. Miwa, A. Fazzio, and J. E. Padilha, ACS Appl. Nano Mater. **2**, 890 (2019).

[40] M. Demirtas, B. Ozdemir, Y. Mogulkoc, and E. Durgun, Phys. Rev. B **101**, 075423 (2020).

[41] A. Kandemir and H. Sahin, Phys. Rev. B **97**, 155410 (2018).

[42] Z. Kahraman, A. Kandemir, M. Yagmurcukardes, and H. Sahin, J. Phys. Chem. C **123**, 4549 (2019).

[43] T. Hu, F. Jia, G. Zhao, J. Wu, A. Stroppa, and W. Ren, Phys. Rev. B **97**, 235404 (2018).

[44] X. Ma, X. Wu, H. Wang, and Y. Wang, J. Mater. Chem. A **6**, 2295 (2018).

[45] W. Kohn and L. J. Sham, Phys. Rev. **140**, A1133 (1965).

[46] P. Hohenberg and W. Kohn, Phys. Rev. **136**, B864 (1964).

[47] G. Kresse and J. Hafner, Phys. Rev. B **47**, 558 (1993).

[48] G. Kresse and J. Hafner, Phys. Rev. B **49**, 14251 (1994).

[49] G. Kresse and J. Furthmüller, Comput. Mater. Sci. **6**, 15 (1996).

[50] G. Kresse and J. Furthmüller, Phys. Rev. B **54**, 11169 (1996).

[51] P. E. Blöchl, Phys. Rev. B **50**, 17953 (1994).

[52] J. P. Perdew, K. Burke, and M. Ernzerhof, Phys. Rev. Lett. **77**, 3865 (1996).

[53] J. Heyd, G. E. Scuseria, and M. Ernzerhof, J. Chem. Phys. **118**, 8207 (2003).

[54] A. V. Krukau, O. A. Vydrov, A. F. Izmaylov, and G. E. Scuseria, J. Chem. Phys. **125**, 224106 (2006).

[55] H. J. Monkhorst and J. D. Pack, Phys. Rev. B **13**, 5188 (1976).

[56] A. Togo and I. Tanaka, Scr. Mater. **108**, 1 (2015).

[57] G. Henkelman, A. Arnaldsson, and H. Jónsson, Comput. Mater. Sci. **36**, 354 (2006).

[58] A. L. Allred, J. Inorg. Nucl. Chem. **17**, 215 (1961).

[59] See Supplemental Material at http://link.aps.org/supplemental/10.1103/PhysRevMaterials.4.114003 for finding more details on ternary alloy configurations, electronic band structures of AlX, orbital projected density of states of AlX/Al$_2XX'$ and strain dependent electronic band structures of AlX/Al$_2XX'$.

[60] L. Lindsay, D. A. Broido, and T. L. Reinecke, Phys. Rev. Lett. **111**, 025901 (2013).

[61] X. Gu and R. Yang, Appl. Phys. Lett. **105**, 131903 (2014).

[62] U. Argaman, R. E. Abutbul, Y. Golan, and G. Makov, Phys. Rev. B **100**, 054104 (2019).

[63] A. J. H. McGaughey, M. I. Hussein, E. S. Landry, M. Kaviany, and G. M. Hulbert, Phys. Rev. B **74**, 104304 (2006).

[64] T. E. Beechem, B. M. Kowalski, M. T. Brumbach, A. E. McDonald, C. D. Spataru, S. W. Howell, T. Ohta, J. A. Pask, and N. G. Kalugin, Appl. Phys. Lett. **107**, 173103 (2015).

[65] O. Del Pozo-Zamudio, S. Schwarz, M. Sich, I. Akimov, M. Bayer, R. Schofield, E. Chekhovich, B. Robinson, N. Kay, O. Kolosov *et al.*, 2D Mater. **2**, 035010 (2015).

[66] Q. Li, Q. Zhou, L. Shi, Q. Chen, and J. Wang, J. Mater. Chem. A **7**, 4291 (2019).

[67] S. Zhou, C.-C. Liu, J. Zhao, and Y. Yao, npj Quant. Mater. **3**, 16 (2018).

[68] O. H. Nielsen and R. M. Martin, Phys. Rev. Lett. **50**, 697 (1983).

[69] Y. Le Page and P. Saxe, Phys. Rev. B **65**, 104104 (2002).

[70] R. C. Andrew, R. E. Mapasha, A. M. Ukpong, and N. Chetty, Phys. Rev. B **85**, 125428 (2012).

[71] I. Frantsevich, F. Voronov, and S. Bokuta, *Elastic Constants and Elastic Moduli of Metals and Insulators Handbook* (Naukova Dumka, Kiev, Ukraine, 1983), pp. 60–180.

[72] A. Pant, Z. Mutlu, D. Wickramaratne, H. Cai, R. K. Lake, C. Ozkan, and S. Tongay, Nanoscale **8**, 3870 (2016).

[73] M. Yagmurcukardes, C. Sevik, and F. M. Peeters, Phys. Rev. B **100**, 045415 (2019).